

Intraplate depth-dependent lithospheric stretching imaged by seismic reflection data

Shuwen Dong (✉ swdong8888@126.com)

Nanjing University

Jianhua Li

Institute of Geomechanics, Chinese Academy of Geological Sciences

Rui Gao

Institute of Geology, Chinese Academy of Geological Sciences

Peter Cawood

Monash University <https://orcid.org/0000-0003-1200-3826>

Hans Thybo

Istanbul Technical University <https://orcid.org/0000-0002-3945-8065>

Yueqiao Zhang

Institute of Geomechanics, Chinese Academy of Geological Sciences

Stephen Johnston

University of Alberta <https://orcid.org/0000-0002-7384-0890>

Jinming Wang

Institute of Geomechanics, Chinese Academy of Geological Sciences

Article

Keywords: seismic reflection profile, kinematic decoupling, mechanically stratified lithosphere

Posted Date: August 18th, 2021

DOI: <https://doi.org/10.21203/rs.3.rs-733095/v1>

License:  This work is licensed under a Creative Commons Attribution 4.0 International License.

[Read Full License](#)

1
2
3
4
5
6
7
8
9
10
11
12
13
14
15
16
17
18
19
20
21
22
23
24

Intraplate depth-dependent lithospheric stretching imaged by seismic reflection data

Shuwen Dong^{1,2,*}, Jianhua Li^{3*}, Rui Gao⁴, Peter A. Cawood⁵, Hans Thybo⁶, Yueqiao Zhang¹, Stephen T. Johnston⁷, Jinming Wang³

¹ *State Key Laboratory for Mineral Deposits Research, Nanjing University, Nanjing 210023, China*

² *SinoProbe Center, Chinese Academy of Geological Sciences, Beijing 100037, China*

³ *Key Laboratory of Paleomagnetism and Tectonic Reconstruction, Ministry of Natural Resources, Institute of Geomechanics, Chinese Academy of Geological Sciences, Beijing 100081, China*

⁴ *School of Earth Science and Geological Engineering, Sun Yat-sen University, Guangzhou, 510275, China*

⁵ *School of Earth, Atmosphere & Environment, Monash University, Melbourne, VIC 3800, Australia*

⁶ *Eurasia Institute of Earth Sciences, Istanbul Technical University, Istanbul, Turkey*

⁷ *Earth and Atmospheric Sciences, University of Alberta, Edmonton, Alberta, Canada*

* Corresponding authors:

Shuwen Dong (email: swdong@nju.edu.cn; swdong8888@126.com)

Jianhua Li (email: lijianhua0301@126.com)

25 **Abstract**

26 Geological and geophysical data coupled with numerical simulations have shown that
27 lithospheric extension at passive margins may be classified into three end-member
28 scenarios of pure shear, simple shear, and depth-dependent deformation. However, how
29 lithospheric extension evolves in an intraplate setting remains enigmatic due to lack of
30 reliable constraints on the deep lithospheric architecture. Here we use a seismic reflection
31 profile across the ~800-km-wide Cretaceous intraplate extensional system of South China
32 to illustrate depth-dependent kinematic decoupling of extension in a mechanically stratified
33 lithosphere. The extension was initially distributed in magma-poor conditions as expressed
34 by normal faulting in the upper crust and lower-crustal flow toward the rift axis. Necking
35 of the crust and Moho uplift led to mantle shear-zone formation, lower-crustal flow toward
36 the rift flanks, and deep mantle flow. We demonstrate that the extensional modes vary with
37 decreasing mantle strength from magma-poor to magma-rich domains, as reflected in
38 decreasing crust-mantle decoupling with increased Moho temperatures (T_M), and the
39 replacement of a two-layer (brittle vs ductile) mantle by a fully ductile mantle. These
40 findings reveal a first-order lithospheric configuration of intraplate depth-dependent
41 extension driven by far-field stresses attributable to slab retreat.

42 Extensional overprinting or disruption of contractional tectonics is a common feature
43 of continental lithospheric evolution of the Earth¹. Lithospheric extension involves a
44 variety of geological processes including crustal thinning, magmatism, exhumation, Moho
45 uplift, and mantle convection²⁻⁴, results in vigorous crust-mantle interaction, and promotes
46 hydrothermal circulation. All these processes are vital for shaping the Earth's lithospheric
47 architecture⁵⁻⁷. Despite decades of research on rifted passive margins⁸⁻¹⁰, considerable
48 controversy exists regarding the nature of lithospheric extension, reflected in three
49 competing tectonic models. The pure-shear stretching model, as inferred from
50 mathematical modeling, predicts in situ, coaxial, and horizontal stretching of the crust, with
51 coupled vertical thinning in the mantle lithosphere¹¹ (**Fig. S1**). A modification to this model
52 envisages decoupling of a heterogeneously deforming brittle upper crust from a ductile
53 middle/lower crust with more evenly distributed deformation, leading to two-layer crustal
54 stretching¹². The simple-shear stretching model, linking crustal displacements over discrete
55 areas via a low-angle ($< 30^\circ$), lithosphere-penetrating fault zone, assumes that extension is
56 largely accommodated by non-coaxial faulting along a lithospheric-scale detachment^{1,13}
57 (**Fig. S1**). The depth-dependent stretching model, which focuses on extensional mechanics
58 and rheological behavior, predicts that lithospheric stretching varies with depth and
59 involves mechanical decoupling and ductile flow between strong layers^{9,14,15}. Although
60 these models predict distinct crustal and mantle structures, differentiation among them has
61 been hampered by the lack of high-resolution seismic reflection data. In contrast to
62 abundant studies of hyperextension and extreme crustal thinning in passive margins, little
63 attention has been paid to continental interiors or intraplate regions, where relatively mild
64 extension is induced by far-field effects including slab retreat or rollback. Two key issues

65 remain elusive regarding (1) how the intraplate extensional strain is vertically partitioned
66 within the lithospheric column, and (2) how the extensional modes vary laterally across a
67 broad intraplate system. Addressing these issues has implications for understanding
68 intraplate extension located hundreds of kilometers away from the convergent margin, and
69 for placing enigmatic intraplate extensional processes within the plate tectonic paradigm¹⁶.

70 Here we address these issues through SINOPROBE seismic reflection profiling of the
71 Cretaceous extensional system of South China (**Fig. 1**). This system, extending over 800
72 km inboard of the convergent margin, is as spectacular as the Basin and Range Province in
73 North America¹⁷. It underwent two stages (~140-120 Ma and ~110-80 Ma) of extension
74 (**Fig. S2**) that gave rise to rift basins (~123,000 km²)¹⁸, metamorphic core complexes¹⁹, and
75 voluminous magmatic bodies restricted to eastern South China (~140,000 km²)¹⁸ (**Fig. 1**).
76 Our new seismic observations, beyond the igneous province, suggest a stratified and
77 mechanically decoupled lithosphere that underwent differential stretching via depth-
78 dependent extension in magma-poor conditions. Combined with published seismic
79 reflection data, we elucidate lateral variations in modes of extension across different
80 domains within the broad extensional system, and present a first-order configuration
81 showing how intraplate depth-dependent lithospheric extension is expressed.

82

83 **New seismic reflection data across the extensional system**

84 Seismic processing includes automatic gain control, refraction statics, and migration,
85 cf. **Methods**. Stacked and migrated profiles were used to define reflections (**Fig. S3**);
86 detailed surface geology is given in **Fig. S4**. Line drawings were made from the migrated
87 profile without vertical exaggeration (**Fig. 2a**), to show tectonic events of differing

88 coherency. Detailed descriptions of the seismic reflections are provided in **Appendix 1**.
89 Here we focus on the first-order features to clarify the overall structural framework.

90 The upper and middle crust is characterized by abundant reflections that display
91 lateral variations in geometry and amplitude (**Fig. 2a**), implying heterogeneous strain and
92 changes in structural style along the profile. In the northwestern part, CDPs (Common
93 Depth Points) 22500-24500, contains three NW-dipping reflections (F₁, F₂ and F₃, **Fig. 2a**)
94 that truncate two arcuate packages of laminar reflections (A and B) and which merge into
95 a ~0.5 s-thick, subhorizontal, high-reflective zone (D₁); this pattern corresponds to three
96 NW-dipping thrusts truncating hanging-wall folds and merging into a subhorizontal
97 decollement (D₁), indicative of southeastward thrust imbrication (**Figs. 3a and S4**). Below
98 event D₁, a thin zone of gently, SE-dipping reflections (D₂, at CDPs 24000-27000) steepens
99 upwards, truncates underlying reflections and approaches D₁. Together, D₁ and D₂ form a
100 critical-taper wedge accommodating contractional strain transfer between the upper and
101 middle crust (**Fig. 3**). Comparable contraction-related features prevail in the southeastern
102 part of the section. Therein three mid-crustal reflections (D₃, D₄ and D₅) exhibit flat-ramp-
103 flat stair-step trajectories (**Fig. 2a**). Sudden changes in reflection dip occur across the ramps,
104 where underlying (footwall) subhorizontal reflections are truncated by the ramps, whereas
105 overlying reflections are parallel to the ramps (hanging-wall flats) (**Fig. 2a**). Folding of
106 hanging-wall reflectors forms thrust-ramp folds. The overall pattern of these reflections
107 resembles a thin-skinned thrust-and-fold system with multiple decollements (**Fig. 3**).

108 These contractional systems are truncated by normal faults, which are seismically
109 manifested as diffractive zones that (1) bound hanging-wall, wedge-shaped reflections
110 corresponding to Cretaceous growth strata within half grabens (F₁₀ and F₁₁, **Fig. 2a**); or (2)

111 displace laterally coherent reflections with normal-sense offsets (F_{12} and F_{13}). The central
112 part of the section (CDPs 26500-29500) is characterized by extension-related reflections
113 defining the Hengyang Basin, manifested by laminar, gentle-dipping reflections that are
114 truncated by a series of conjugate normal faults (**Fig. 2b**), corresponding to Cretaceous
115 strata deformed by distributed normal faulting (**Fig. 3**). The basin is underlain by a domain
116 almost devoid of reflections that truncates mid-crustal contractional systems to the NW
117 and SE (**Fig. 2a**), suggesting that the thermal-mechanical extensional tectonism has almost
118 completely overprinted the compressional structures below the Hengyang Basin.

119 The lower crust is attenuated and highly reflective (**Fig. 2a**). Although the reflectivity
120 changes character slightly in amplitude and coherence, it is characterized by finely-
121 laminated, subhorizontal reflections with a thickness (measured in two-way time) of 4-5s
122 extending across the entire section (Lc in **Figs. 2c, d**). Bands of gently dipping (20-30°)
123 sets of SE-dipping reflections (S_1 and S_2) occur between the subhorizontal reflection bands,
124 giving the impression of parallel arrays of high-strain structures (**Figs. 2c, d**).

125 The Moho (M) is imaged as the transition between the highly reflective lower crust
126 and the largely transparent upper mantle. The Moho shows long-wavelength deformation,
127 rising to 11 s below the Hengyang Basin from depths of 12-12.5 s (**Fig. 2a**) in the
128 surrounding region, indicating a variation of crustal thickness in the order of 1-1.5 s (3-4.5
129 km).

130 Below the Moho, the most striking feature is a conjugate set of three gently dipping
131 (20-30°), highly reflective zones that extend down from Moho to ~13 s depth within an
132 otherwise seismically transparent mantle (**Fig. 2e**). These reflection zones dip away from
133 the centre of the Moho uplift on both sides.

134 **Intraplate depth-dependent stretching of stratified lithosphere**

135 Our analysis of seismic reflection data leads to the following first-order observations
136 (**Figs. 3 and S5**). First, the upper and middle crustal reflections suggest an overall structural
137 architecture of crustal shortening extensively modified by normal faults due to subsequent
138 extension. Second, the lower crust shows pervasive, finely-laminated, subhorizontal
139 reflections around groups of inclined reflections (S_1 and S_2). Third, the Moho is smooth
140 and continuous, and shows an upward arching spatially associated with upper-crustal
141 normal faults, reflecting the locus of crustal necking; the thinnest crust is immediately
142 beneath the Hengyang basin. Fourth, conjugate high-amplitude reflections dip away from
143 the centre of the Moho uplift in an otherwise transparent upper mantle.

144 We interpret the lower-crustal reflections to represent a combination of two end-
145 member hypotheses, i.e., strain-related banding due to extensive ductile flow within a
146 rheologically weak lower crust^{20,21}, and localized mafic sills or intrusions^{22,23}. Wide-angle
147 seismic data of the lower crust indicate a P-wave velocity of 6.5-6.8 km/s lower than that
148 (> 7.0 km/s) of mafic-ultramafic lower crust²⁴, confirming an overall more felsic and hence
149 weaker lower crust. Therein the finely laminated reflections likely reflect a pervasive
150 mylonitic foliation formed by simple-shear deformation during channelized flow^{20,25}. The
151 presence of localized mafic sills are consistent with two lines of evidence: (1) the lower
152 crust shows localized zones of high reflectivity concentrated in distinct bands (H_1 - H_3 , **Fig.**
153 **2a**); and (2) surface exposures of mafic dikes and basalts show high $\epsilon_{Nd}(t)$ values (-2.2 to
154 7.2) and low La/Nb ratios (0.59 to 1.59)²⁶. Such evidence demonstrates localized mantle
155 underplating and influx in the form of layered mafic sills within a more felsic lower crust.
156 Gentle to moderate S_1 and S_2 foliations may represent imbricated, anastomosing shear

157 zones that alternate with low-strain domains, i.e., highly deformed and sheared zones
158 surrounding undeformed, transparent areas²⁵. They resemble S-foliations at small angles
159 to the subhorizontal shear bands (i.e., C-foliations) within major shear zones (**Fig. 3**). This
160 spatial relationship probably represents constructive interference of small-scale seismic
161 signals which, nevertheless, preserve the overall structure originating from ductile shearing
162 and plastic deformation during lower-crustal flow. The recognition of channelized flow
163 supports the interpretation that the weakest layer of the continental lithosphere resides in
164 the lower crust, not, as is commonly assumed, in the middle crust²⁷. One further issue
165 concerns the direction of flow. By incorporating results from numerical simulations^{10,15},
166 we suggest two stages of flow due to buoyancy-driven forces caused by crustal and mantle
167 lithosphere thinning, respectively. The initial flow was inward toward the rift axis (① in
168 **Fig. 3**), driven by a lateral pressure gradient created by localized thinning of the upper
169 crust²⁸, a mechanism akin to that responsible for the formation of metamorphic core
170 complexes²⁹. As extension and thinning continue, increased mantle-dominated buoyancy
171 forces, including mantle lithosphere thinning, Moho uplift and asthenospheric upwelling¹⁰,
172 reversed the flow direction and drove the lower crust to flow outwards toward the rift flanks
173 (② in **Fig. 3**). The channelized flow mechanically decoupled upper-middle crustal
174 deformation from mantle deformation. The decoupling pattern, manifested by individual
175 stretching of upper crust and upper mantle about the same rift axis (**Fig. S5**), indicates
176 diffuse decoupling³⁰. Studies on governing equations demonstrate that such decoupling
177 occurs when the ratio of $u_p \cdot h_0 / k_{cf} < 100$ (k_{cf} , the diffusion constant; u_p , the plate spreading
178 velocity; h_0 , the crustal thickness)³⁰. We calculate the initial Moho temperature (T_M) of the
179 study area by plotting $\log(u_p \cdot h_0 / k_{cf})$ vs T_M using the equations from refs. 30, 31 (**Table S1**).

180 Results suggest that, for both wet and dry ~40 km thick quartz crust, the diffuse decoupling
181 herein occurred at $T_M \sim 440\text{-}640\text{ }^\circ\text{C}$ (**Fig. S6**), comparable to that of non-volcanic passive
182 margins³².

183 We interpret the mantle reflectors as ductile shear zones that reflect strain localization
184 in the uppermost mantle (**Fig. 3**), because (1) mantle strain localization involves grain size
185 reduction in olivine³³ that can decrease viscosity and cause attenuation of seismic shear
186 waves³⁴; and (2) the layering of mantle mylonites can cause differential acoustic
187 impedances and hence high reflectivity³⁵. Similar mantle shear zones have been reported
188 beneath other continental rifts (e.g., the North Sea Basin in Europe)^{36,37}. They generally
189 initiate in the crustal necking stage when strain in the crust and mantle begins to link¹⁴, and
190 accommodate large-scale displacement away from the mantle dome^{14,27}. We infer that
191 these shear zones control the exhumation and ascent of the deeper mantle; such shear zones
192 were reproduced in analogue models of mantle exhumation at passive margins²⁹.

193 The imaged lower-crustal flow and mantle shear-zone formation are interpreted as
194 concomitant Cretaceous extensional features, because: (1) they show well-defined spatial
195 association and kinematic consistency with upper-crustal Cretaceous normal faults and the
196 Moho uplift, respectively; and (2) seismic profiling primarily images structures attributable
197 to the most recent and intensive tectonic event affecting the crust³⁸, herein corresponding
198 to the remarkable Cretaceous extensional event. Despite the synchronism of crustal and
199 mantle extension, discrepancies exist regarding the amounts and modes of extension both
200 within the crust and between the crust and mantle. Specifically, although the upper and
201 lower crust underwent extension across a wide region, upper crustal extension was
202 characterized by localized thinning via normal faulting, whereas the lower crust was

203 stretched by channelized flow but in a more distributed fashion across the entire section
204 (**Fig. 3**). That said, the magnitude of stretching ($\beta x = \text{extended length of crust/original}$
205 length of crust)³⁹ and attenuation ($\delta x = 1 - 1/\beta x$)⁶ are broadly comparable; 1.0 - 1.40 and 0.0
206 - 0.29 for the upper crust versus 1.0 - 1.22 and 0.0 - 0.18, for the lower crust, respectively
207 (**Fig. 3**). In contrast to wide-scale distributed extension through the crustal profile, the
208 localized mantle shear zones focused the upper-mantle thinning in a much narrower zone
209 (**Fig. 3**). Such extension discrepancies suggest depth-dependent differential stretching of
210 the upper lithosphere.

211 To explore the effect of extension on the lower lithosphere, we determine deformation
212 patterns of the mantle lithosphere from seismic anisotropy⁴⁰, based on a compilation of
213 shear-wave splitting measurements in South China⁴¹. The directions of mantle seismic
214 anisotropy suggest dominant NW-SE-orientated flow of the mantle lithosphere (**Fig. 4a**).
215 Although the fabrics beneath western South China reflect Cenozoic mantle flow
216 accommodating recent eastward expansion of the Tibetan Plateau⁴², eastern South China
217 has been subject to negligible Cenozoic deformation⁴³ and hence mantle fabrics are mostly
218 ‘fossil’ signals that are relics of Cretaceous flow. The NW-SE flow direction is parallel to
219 the stretching lineation of metamorphic core complexes (**Fig. 4b**) consistent with dominant
220 lower-crustal flow during extension⁴⁴. The remarkable parallelism demonstrates that the
221 lower crust and mantle lithosphere flowed in the same direction during lithospheric
222 stretching (**Fig. 4a**). The flow direction is consistent with regional NW-SE-oriented
223 extensional stresses (**Fig. 4a, b**) that dominated the opening of upper-crustal basins¹⁹.

224 The above observations differ from the predictions of the simple-shear and pure-shear
225 hypotheses. First, the differential stretching of the lithosphere, coupled with depth-

226 dependent stretching and attenuation factors, is inconsistent with the uniform extension
227 predicted by the simple-shear model¹¹. Second, the absence of a lithosphere-penetrating
228 reflection zone is incompatible with the simple-shear model^{1,13} on predicting
229 accommodation of lithospheric extension along a single low-angle detachment. Instead,
230 our observations support a four-layer stratified lithosphere that was stretched by depth-
231 dependent extension in magma-poor conditions (**Fig. 5a**). The extension appears to
232 comprise two successive stages with respect to initiation and amplification. First,
233 distributed thinning of the upper crust by normal faulting (A, **Fig. 5a**) was matched by
234 lower-crustal flow toward the rift axis to compensate for upper-crustal thinning (B) and
235 possible slight exhumation of upper mantle (C). This initial stage was followed by crustal
236 necking capable of generating an arched Moho (D), localized mantle exhumation prompted
237 by mantle shear-zone formation (E), lower-crustal flow toward the rift flanks (F) and
238 mantle influx into the crust in the form of mafic sills (G), and mantle flow (H) possibly
239 accompanied by small-scale mantle necking and upwelling/convection (I) as illustrated by
240 the geochemistry of coeval basalt²⁶ and by laboratory experiments⁴⁵.

241 **Lateral variation in modes of depth-dependent extension**

242 To elucidate lateral variation in modes of depth-dependent extension, we reconstruct
243 the overall architecture of the broad (~800-km-wide) intraplate extension driven by slab
244 retreat (**Fig. 5b**), by integrating the complete > 1000-km-long seismic reflection data across
245 South China^{43,46} (**Fig. 1**). Based on the distribution of compressional/extensional structures
246 and magmatic activity, we define three domains, a western pre-rift domain, a central
247 magma-poor domain, and an eastern magma-rich domain (**Fig. 5b**). The pre-rift domain
248 shows a thick, stratified crust that lacks any Cretaceous thermal perturbations⁴⁶ (**Fig. 5b**).

249 The presence of a high-viscosity lower crust requires vertically coherent deformation (e.g.,
250 the thin-viscous-sheet model⁴⁷), and precludes large rheological contrasts and lower-crustal
251 flow within the lithosphere, implying crust-mantle coupling at low $T_M < 480$ °C³². In
252 contrast to the central magma-poor domain (**Fig. 5a**), the eastern magma-rich domain⁴³
253 shows different extensional characteristics, including (**Fig. 5b**): upper-crustal normal
254 faulting and dilation by magmatic injection (A); lower-crustal flow and melting (B);
255 basaltic underplating (C); mantle influx into the lower crust in the form of layered mafic
256 sills (D); Moho shallowing by 2-4 km (E); partial melting in the mantle lithosphere (F);
257 and asthenospheric upwelling (G). Extensive lower-crustal partial melting implies a high
258 $T_M > 700$ °C³²; this was reflected in decreased crustal-mantle decoupling, due to the
259 absence of a high-strength mantle at high temperatures³². From pre-rift to magma-poor
260 domains, regional extension caused a transition from a coupled to a decoupled style of
261 lithospheric deformation associated with increasing T_M , due to rheological weakening of
262 the lower crust (**Fig. 5b**). From magma-poor to magma-rich domains, the extension seems
263 to be facilitated by magmatism, and involves the following variations: (1) the replacement
264 of a two-layer (brittle vs ductile) mantle lithosphere by a wholly ductile mantle lithosphere;
265 (2) marked decreases in the mantle strength and crust-mantle decoupling; (3) an increase
266 in the T_M ; and, (4) the abandonment of mantle shear zones due to intense mantle melting
267 and basaltic underplating (**Fig. 5b**). These lateral variations may originate from thermal
268 perturbation of the mantle by deeper asthenospheric upwelling. Our observations reveal
269 how intraplate lithospheric extension can be characterized in a general depth-dependent
270 architecture as a first-order configuration. This configuration provides a basis for
271 discussing modes of lithospheric extension in intraplate or other complex tectonic settings,

272 such as wide versus narrow rifting^{5,29,32}, extreme tectonic decoupling, and large-scale
273 lateral offset between upper-crustal and mantle-lithospheric extensions in the Basin and
274 Range province, USA⁴⁸.

275

276 **Methods**

277 **DATA ACQUISITION**

278 The seismic data were acquired by using Sercel SN408XL 24-bit digital seismic
279 recorders with 1600 channels. Dynamite sources of 40 kg nominal for normal shots and
280 200 kg nominal for large shots were fired with a spacing of 160 m and 5000 m, respectively.
281 Shot spacing was reduced to 80 m across the mountainous regions. Dynamite for 40-kg
282 sources was placed in single holes at depth of 22-24 m. Dynamite for 200-kg sources were
283 detonated in 25-m deep 5-hole arrays. SM-24 geophones were used with a dominant
284 frequency of 10-Hz in a group space of 40 m. Seismic data were recorded for 30s at a
285 sampling rate of 2 ms. The acquisition parameters are listed in Table S2 below.

286 Table S2 Acquisition parameters for improved standard oil-industry

287 Shot interval 160 m nominal for Normal shot (Basin)

288 80 m nominal for Normal shot (orogen)

289 5000m nominal for Large shot

290 Source Dynamite

291 Charge size 40 kg nominal for Normal shot

292 200 kg nominal for Large shot

293 Shot depth 22 m ×2 for Normal shot (40 kg)

294 25 m×5 for Large shot (200 kg)

295 Nominal fold 60 (Basin)
296 120 (Orogen)
297 Geophone type SM24-10Hz
298 Number of groups 480
299 Group interval 40 m
300 Geophone array 12 geophones in 11 m linear array
301 Near offset 20m (Normal shot)
302 140m (Large shot)
303 Far offset 9580m (Normal shot)
304 19300m (Large shot)
305 Spread symmetric split (Normal shot)
306 End-on (Large shot)
307 Sample rate 2 ms
308 Record length 30 s
309 Low-cut filter 15 Hz
310 High-cut filter 250Hz
311 Notch filters out
312 Layout type: 9580-20-40-20-9580 (Normal shot)
313 0-0-40-140-19300 (Large shot)

314

315 **DATA PROCESSING**

316 (1) Routine Processing

317 By combining the advantages of Grisys, Omega and CGG systems, we conducted seismic
318 processing following a standard procedure generally practiced in the petroleum industries.

319 These include the key steps using the following software packages: Demultiplex, Geometry
320 Definition, Record & Trace Edition, Stacking Area Element Parameters Chosen (for
321 crooked lines), Editing/Muting, Gain Recovery, Elevation Static, Spectral Analysis,
322 Bandpass Filtering, Velocity Analysis, Normal Moveout Correction (NMO), Residual
323 Static Correction, and Stacking and Migration.

324 Muting was accomplished by applying a fixed amplitude recovery (spherical divergence
325 and balance) designed to keep the trace amplitudes roughly constant with time and across
326 the shot records. In this way, any traces contaminated by environmental noise (wind, cattle,
327 traffic) stood out and are expressed as high-amplitude traces at depth. This is because the
328 recorded amplitude of the noise is more or less constant with time (whereas the amplitudes
329 of the seismic reflections decrease rapidly with time) and the spherical divergence
330 correction (designed to even out the seismic signal) greatly amplifies the noise. Once this
331 was done, it became straightforward to mute the noise signals from the shot records using
332 an interactive display.

333 A replacement velocity of 4000 m/s and a reference elevation of 1200 m have been used
334 to calculate the elevation and static corrections. First breaks were picked manually.
335 Effective reflectivity has a bandwidth of 5 to 45 Hz and dominant frequency of 22 Hz. A
336 wider pass-band was used for the pre-stack data. For the top 2.5 s TWT the filter
337 specifications were (8-12-65-70Hz).

338 After band-pass filtering and a CMP gather, elevation and statics were applied. For
339 uplifting signal-noise ratio, Pre-stack F-K filtering and Wiener deconvolution were tested
340 but found not to improve the data significantly, and so were not applied to the data. Velocity
341 analyses were performed, but below 6 s the normal moveout correction is almost senseless

342 for the velocity variation. Surface-consistent residual statics were calculated by STACK-
343 POWER method interactively with the velocity analyses. Automatic gain control, F-K filter
344 to attenuate steeply dipping events and pre-stack time migration was performed. The
345 sections are plotted with no vertical exaggeration for a velocity of 6 km/s.

346 (2) Special Processing Procedures

347 Traditional refraction methods could provide satisfactory static correction results for near-
348 surface layered structures. However, the first arrivals of shot data may be highly distorted
349 due to severe topography and rapidly variable near-surface structures. Refraction static and
350 ray-tracing tomography methods were tested but they did not help improve the data quality.
351 Instead, we apply the TSCWR technique that solves nonlinear wave equations using a
352 finite-difference method. This method was combined with the first wave's stability and the
353 flexibility of rotary to avoid the shadow effect behind high-velocity bodies. TSCWR
354 performance is faster and better in static correction than refraction and ray-tracing
355 tomography for same shot data.

356 The common pre-stack processing of commercial software packages (e.g., CGG and
357 PROMAX) and wave-equation and line-migration techniques were attempted on the
358 seismic data acquired from the mountainous areas, but the results show low signal-to-noise
359 ratios. This problem was overcome by applying an improved algorithm of Kirchhoff Pre-
360 Stack Time Migration in rough Earth surface (KPSTM), which is pending for a patent in
361 China.

362 **Data availability**

363 The authors declare that all data supporting the findings of this study are available within the
364 main text, figures and Supplementary Information files.

365 **References**

- 366 1. Wernicke, B. Low-angle normal faults in the Basin and Range Province: nappe tectonics in an
367 extending orogen. *Nature* **291**, 645–648 (1981).
- 368 2. Brun, J. P. & Wenzel, F. Crustal-scale structure of the southern Rhinegraben from ECORS-DEKORP
369 seismic reflection data. *Geology* **19**, 758-762 (1991).
- 370 3. KRISP Working Party. Large-scale variation in lithospheric structure along and across the Kenya
371 rift. *Nature* **354**, 223–227 (1991).
- 372 4. Thybo, H. & Nielsen, C. A. Magma-compensated crustal thinning in continental rift zones. *Nature*
373 **457**, 873–876 (2009).
- 374 5. Buck, W. R. Modes of continental lithospheric extension. *Journal of Geophysical Research* **96**,
375 20161-20178 (1991).
- 376 6. Huisman, R. S. & Beaumont, C. Complex rifted continental margins explained by dynamical
377 models of depth-dependent lithospheric extension. *Geology* **36**, 163–166 (2008).
- 378 7. Burov, E. & Gerya, T. Asymmetric three-dimensional topography over mantle plumes. *Nature* **513**,
379 85–89 (2014).
- 380 8. Beach, A. A deep seismic reflection profile across the northern North Sea. *Nature* **323**, 53–55 (1986).
- 381 9. Huisman, R. & Beaumont, C. Depth-dependent extension, two-stage breakup and cratonic
382 underplating at rifted margins. *Nature* **473**, 74–78 (2011).
- 383 10. Brune, S., Heine, C., Pérez-Gussinyé, M. & Sobolev, S. V. Rift migration explains continental
384 margin asymmetry and crustal hyper-extension. *Nat Commun* **5**, 4014 (2014).
- 385 11. McKenzie, D. Some remarks on the development of sedimentary basins. *Earth and Planetary*
386 *Science Letters* **40**, 25-32 (1978).
- 387 12. Gans, P. B. An open-system, two-layer crustal stretching model for the Eastern Great Basin.
388 *Tectonics* **6**, 1-12 (1987).
- 389 13. Wernicke, B. Low-angle normal faults and seismicity: a review. *Journal of Geophysical Research*
390 *Solid Earth* **100**, 20159-20174 (1995).
- 391 14. Weinberg, R. F., Regenauer-Lieb, K. & Rosenbaum, G. Mantle detachment faults and the breakup

- 392 of cold continental lithosphere. *Geology* **35**, 1035-1038 (2007).
- 393 15. Huisman, R. S. & Beaumont, C. Rifted continental margins: the case for depth-dependent
394 extension. *Earth & Planetary Science Letters* **407**, 148-162 (2014).
- 395 16. Dyksterhuis, S. & Müller, R. D. Cause and evolution of intraplate orogeny in Australia. *Geology* **36**,
396 495-498 (2008).
- 397 17. Dickinson, W. R. The Basin and Range Province as a Composite Extensional Domain. *International*
398 *Geology Review* **44**, 1-38 (2002).
- 399 18. Zhou, X., Sun, T., Shen, W., Shu, L. & Niu, Y. Petrogenesis of Mesozoic granitoids and volcanic
400 rocks in South China: a response to tectonic evolution. *Episodes* **29**, 26-33 (2006).
- 401 19. Li, J.H., Zhang, Y.Q., Dong, S.W. & Johnston, S.T. Cretaceous tectonic evolution of South China: a
402 preliminary synthesis. *Earth-Sci. Rev.* **134**, 98-136 (2014).
- 403 20. Hurich, C. A., Smithson, S. B., Fountain, D. M. & Humphreys, M. C. Seismic evidence of mylonite
404 reflectivity and deep structure in the Kettle dome metamorphic core complex,
405 Washington. *Geology* **13**, 577-580 (1985).
- 406 21. Reston, T. J. Evidence for shear zones in the lower crust offshore Britain. *Tectonics* **7**, 929-945
407 (1988).
- 408 22. McKenzie, D. A possible mechanism for epeirogenic uplift. *Nature* **307**, 616–618 (1984).
- 409 23. Lyngsie, S.B., Thybo, H. & Lang, R. Rifting and lower crustal reflectivity: A case study of the
410 intracratonic Dniepr-Donets rift zone, Ukraine. *Journal of Geophysical Research* **112**, 1-27 (2007).
- 411 24. Zhang, Z., Xu, T., Zhao, B. & Badal, J. Systematic variations in seismic velocity and reflection in
412 the crust of Cathaysia: new constraints on intraplate orogeny in the South China
413 continent. *Gondwana Research* **24**, 902–917 (2013).
- 414 25. Abramovitz, T., Berthelsen, A. & Thybo, H. Proterozoic sutures and terranes in the southeastern
415 Baltic Shield interpreted from BABEL deep seismic data. *Tectonophysics* **270**, 259-277 (1997).
- 416 26. Meng, L. F., Li, Z. X., Chen, H. L., Li, X. H. & Wang, X. C. Geochronological and geochemical
417 results from Mesozoic basalts in southern South China Block support the flat-slab subduction
418 model. *Lithos* **132**, 127-140 (2012).

- 419 27. Nagel, T. J. & Buck, W. R. Symmetric alternative to asymmetric rifting models. *Geology* **32**, 937-
420 940 (2004).
- 421 28. Block, L. & Royden, L. H. Core complex geometries and regional scale flow in the lower
422 crust. *Tectonics* **9**, 557-567 (1990).
- 423 29. Brun, J. P., Sokoutis, D., Tirel, C., Gueydan, F. & Beslier, M. O. Crustal versus mantle core
424 complexes. *Tectonophysics* **746**, 22-45 (2018).
- 425 30. Hopper, J. R. & Buck, W. R. Styles of extensional decoupling. *Geology* **26**, 699-702 (1998).
- 426 31. Hopper, J. R. & Buck, W. R. The effect of lower crustal flow on continental extension and passive
427 margin formation. *Journal of Geophysical Research Solid Earth* **101**, 20175-20194 (1996).
- 428 32. Gueydan, F., Morency, C. & Brun, J. P. Continental rifting as a function of lithosphere mantle
429 strength. *Tectonophysics* **460**, 83-93 (2008).
- 430 33. Kirby, S. H. Rock mechanics observations pertinent to the rheology of the continental lithosphere
431 and the localization of strain along shear zones. *Tectonophysics* **119**, 1-27 (1985).
- 432 34. Lavier, L. L. & Manatschal, G. A mechanism to thin the continental lithosphere at magma-poor
433 margins. *Nature* **440**, 324-328 (2006).
- 434 35. Frederiksen, S. & Braun, J. Numerical modelling of strain localisation during extension of the
435 continental lithosphere. *Earth & Planetary Science Letters* **188**, 241-251 (2001).
- 436 36. Klemperer, S. L., Hauge, T. A., Hauser, E. C., Oliver, J. E. & Potter, C. J. The Moho in the northern
437 Basin and Range province, Nevada, along the COCORP 40°n seismic-reflection
438 transect. *Geological Society of America Bulletin* **97**, 603-618 (1986).
- 439 37. Klemperer, S. L. Crustal thinning and nature of extension in the northern North Sea from deep
440 seismic reflection profiling. *Tectonics* **7**, 803-821(1988).
- 441 38. Burg, J. P., Sokoutis, D. & Bonini, M. Model-inspired interpretation of seismic structures in the
442 Central Alps: Crustal wedging and buckling at mature stage of collision. *Geology* **30**, 643-646
443 (2002).
- 444 39. Daley, E. E. & DePaolo, D. J. Isotopic evidence for lithospheric thinning during extension:
445 Southeastern Great Basin. *Geology* **20**, 104-108 (1992).

- 446 40. Brun, J. P. & Sokoutis, D. 45 m.y. of Aegean crust and mantle flow driven by trench retreat. *Geology*
447 **38**, 815-818(2010).
- 448 41. Huang, Z. C., Wang, L. S., Zhao, D. P., Mi, N. & Xu, M. J. Seismic anisotropy and mantle dynamics
449 beneath China. *Earth & Planetary Science Letters* **306**, 105-117 (2011).
- 450 42. Wang, C. Y., Flesch, L. M., Silver, P. G., Chang, L. J. & Chan, W. W. Evidence for mechanically
451 coupled lithosphere in central Asia and resulting implications. *Geology* **36**, 363-366 (2008).
- 452 43. Dong, S. W., Li, J. H., Cawood, P. A., Gao, R., Zhang, Y.Q. & Xin, Y.J. Mantle influx compensates
453 crustal thinning beneath the Cathaysia Block, South China: Evidence from SINOPROBE
454 reflection profiling. *Earth and Planetary Science Letters* **544**, 116360 (2020).
- 455 44. Costa, S. & Rey, P. Lower crustal rejuvenation and growth during post-thickening collapse: insights
456 from a crustal cross section through a Variscan metamorphic core complex. *Geology* **23**, 905-908
457 (1995).
- 458 45. Mondy, L. S., Rey, P. F., Duclaux, G. & Moresi, L. The role of asthenospheric flow during rift
459 propagation and breakup. *Geology* **46**, 103-106(2018).
- 460 46. Li, J. H., Dong, S. W., Cawood, P. A., Zhao, G. C., Johnston, S. T., Zhang, Y. Q. & Xin, Y. J. An
461 Andean-type retro-arc foreland system beneath northwest South China revealed by SINOPROBE
462 profiling. *Earth & Planetary Science Letters* **490**, 170-179(2018).
- 463 47. England, P. & Houseman, G. Finite strain calculations of continental deformation: 2. Comparison
464 with the India-Asia Collision Zone. *Journal of Geophysical Research Solid Earth* **91**, 3664-3676
465 (1986).
- 466 48. Schulte-Pelkum, V., Biasi, G., Sheehan, A. & Jones, C. Differential motion between upper crust and
467 lithospheric mantle in the central Basin and Range. *Nature Geosci* **4**, 619–623 (2011).
- 468 49. Li, J. H., Cawood, P. A., Ratschbacher, L., Zhang, Y. Q., Dong, S. W., Xin, Y. J., Yang, H. & Zhang,
469 P.X. Building Southeast China in the late Mesozoic: insights from alternating episodes of
470 shortening and extension along the Lianhuashan fault zone. *Earth-Sci. Rev* **201**, 1-29 (2020).
- 471 50. Regenauer-Lieb, K., Weinberg, R. & Rosenbaum, G. The effect of energy feedbacks on continental
472 strength. *Nature* **442**, 67–70 (2006).

473 **Acknowledgements**

474 This work was financially supported by grants from Natural Science Foundation of China
475 (41822205), Sino-Probe (08-01), National Key R&D Program of China
476 (2017YFC0601402). Peter Cawood acknowledges support from Australian Research
477 Council grant FL160100168.

478 **Author contributions**

479 S.D. and J.L. conceived this study. R.G. and S.D. managed the project and supervised
480 data acquisition. J.L., S.D., P.A.C., H.T. and S.T.J. did the data analysis and wrote the
481 manuscript. All of the authors contributed to the data interpretation.

482 **Competing interests**

483 The authors declare no competing financial interests.

484 **Additional information**

485 **Supplementary information** is available in the online version of the paper.

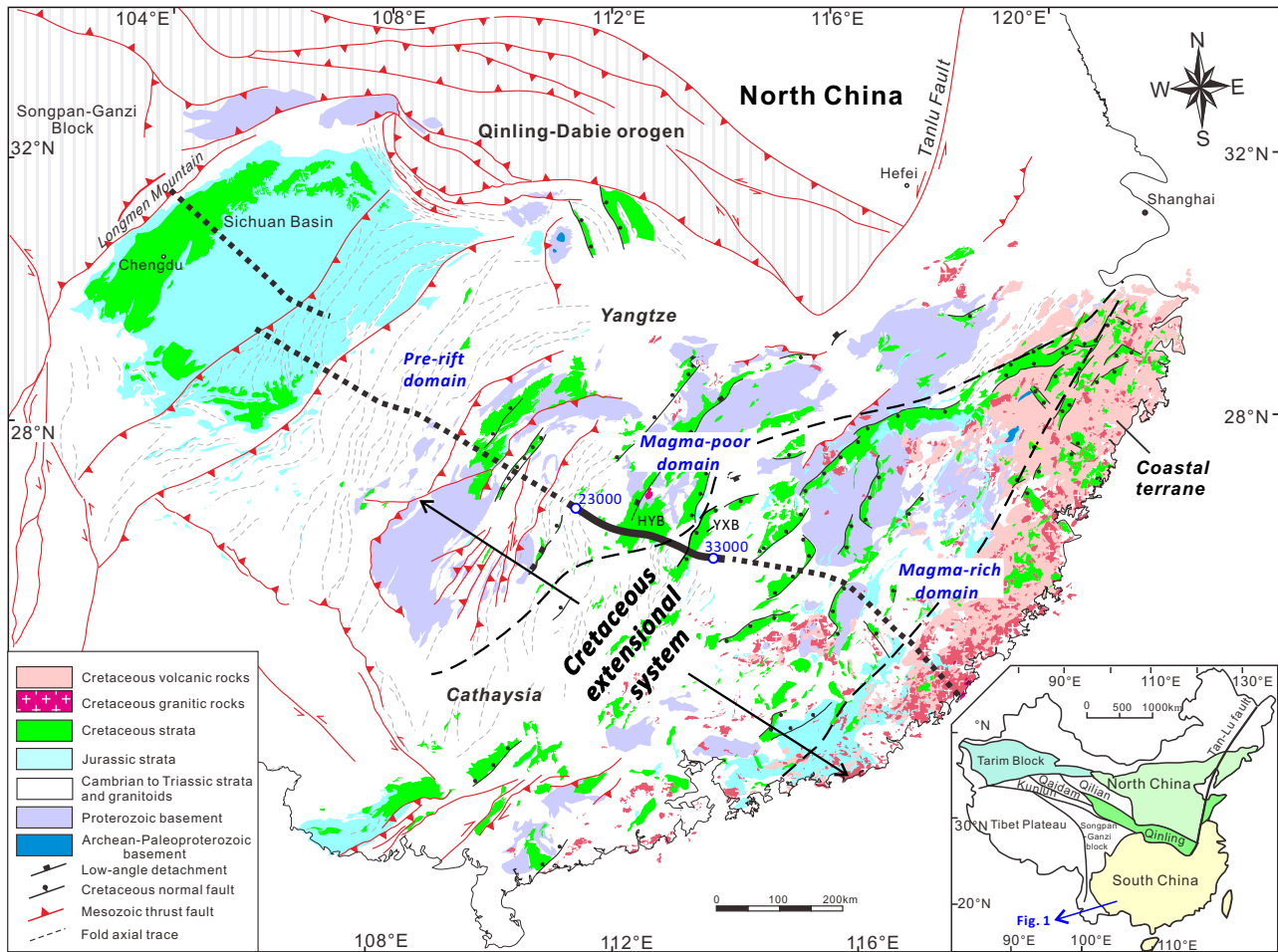


Fig. 1 Geological sketch map of South China. Simplified geologic map showing the extent of the Cretaceous extensional system in South China. The black solid line indicates the seismic line combined to form the cross section in Fig. 2a; the dotted lines indicate other seismic profiles^{43,46} finished by SINOPROBE. Abbreviations: HYB, Hengyang basin; YXB, Yongxing basin. Inset shows the location of South China in the tectonic framework of the People's Republic of China.

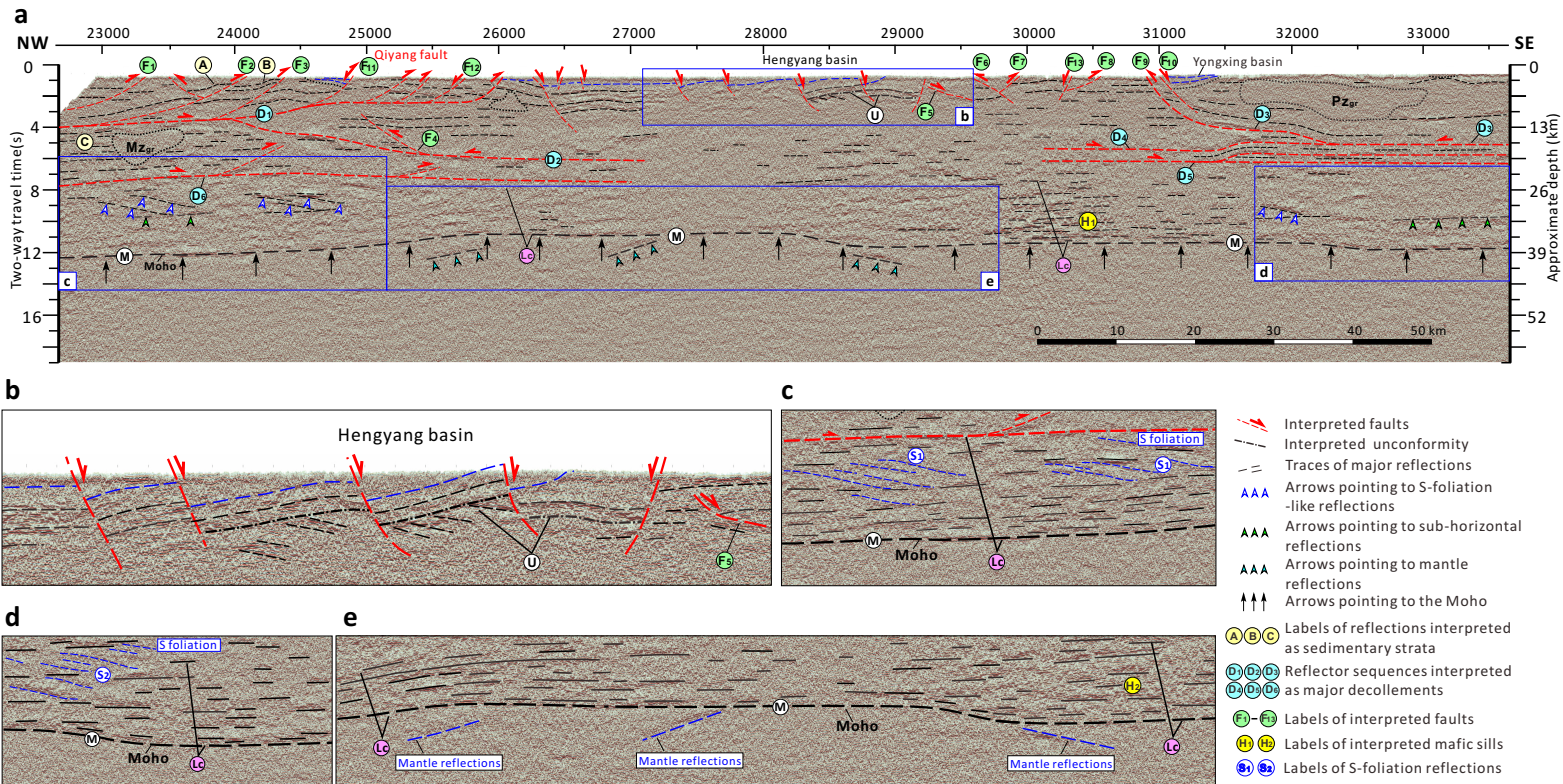


Fig. 2 Seismic reflection images from SINOPROBE across central South China. a, Migrated seismic profile with labels of main geologic features discussed in text. **b-e**, Close-up views. **b**, Seismic profile showing crustal architecture beneath the Hengyang basin. **c and d**, Seismic profiles showing the highly reflective lower crust, in which a pair of gentle-dipping reflections (S_1 and S_2) are sandwiched between subhorizontal reflection bands. **e**, Seismic profile showing the Moho rise and three isolated, gentle-dipping reflective zones in the upper mantle.

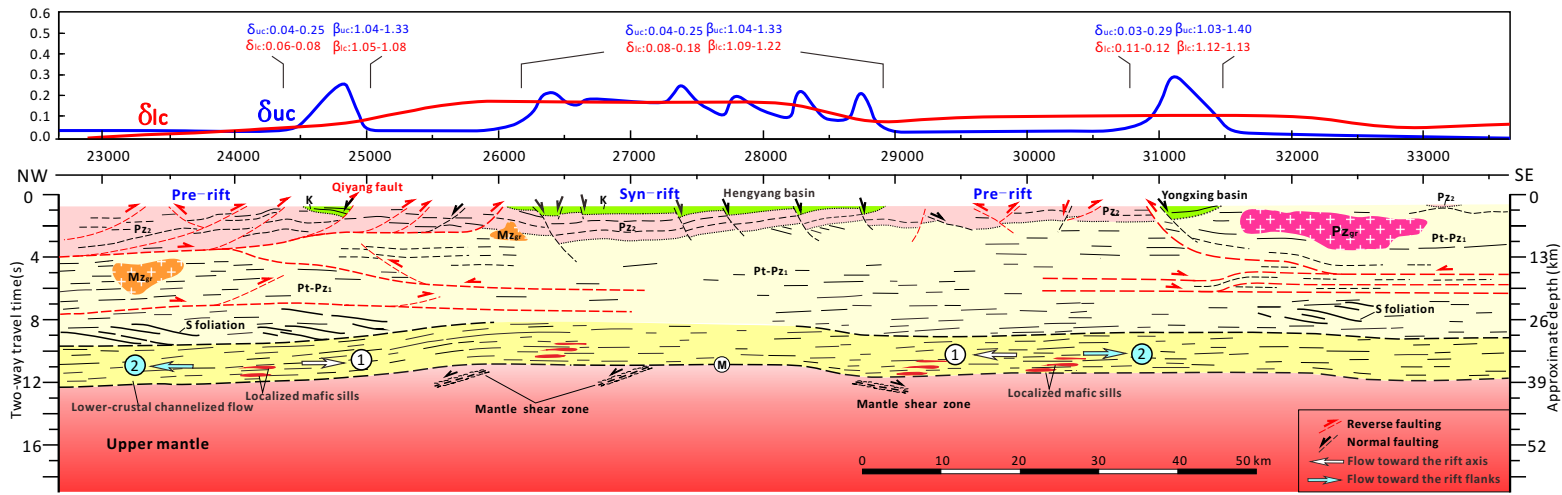


Fig. 3 Interpreted profile and calculated crustal attenuation factors. The lower sub-figure shows interpreted profile. To ensure the plausibility and testability, our interpretations are consistent with surface geology, regional tectonic evolution, existing geophysical constraints, and principles of mass conservation and balance. The upper sub-figure shows plots of upper and lower crustal attenuation factors (δ_{uc} and δ_{ic}) of the profile. The crustal attenuation factor is defined as $\delta_x = 1 - 1/\beta_x$, where β_x , the crustal thinning/stretching factor, is defined as $\beta_x = \text{extended length of crust} / \text{original length of crust}$.

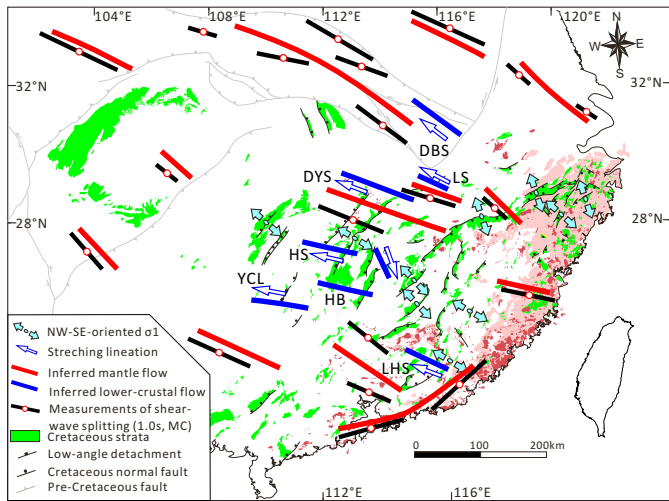
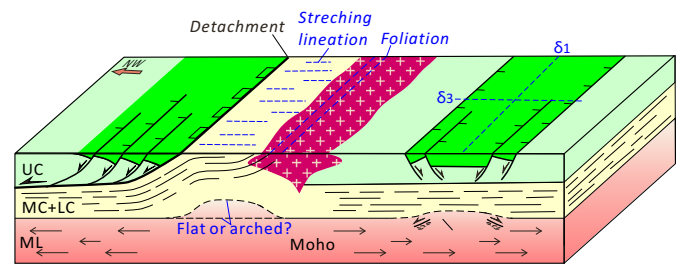
a**b**

Fig. 4 Crustal and mantle flow patterns across the Cretaceous extensional system. **a**, Relationships between directions of stretching in metamorphic core complexes, and of seismic anisotropy in mantle lithosphere. Directions of the stretching lineation within metamorphic core complexes are determined from ref. 49. Abbreviations: DBS, Dabieshan; DYS, Dayunshan; HS, Hengshan; LS, Lushan; TBS, Tongbaishan; GS, Wugongshan; YCL, Yuechengling. The mantle seismic anisotropy is based on a compilation of shear-wave splitting measurements (MC method) from the XKS phases in ref. 41. Determinations of paleo-tectonic stress fields are from ref. 19. **b**, A cartoon showing the relation between surface stretching lineation and deep crustal flow. Abbreviations: UC, upper crust; MC, middle crust; LC, lower crust; ML, mantle lithosphere.

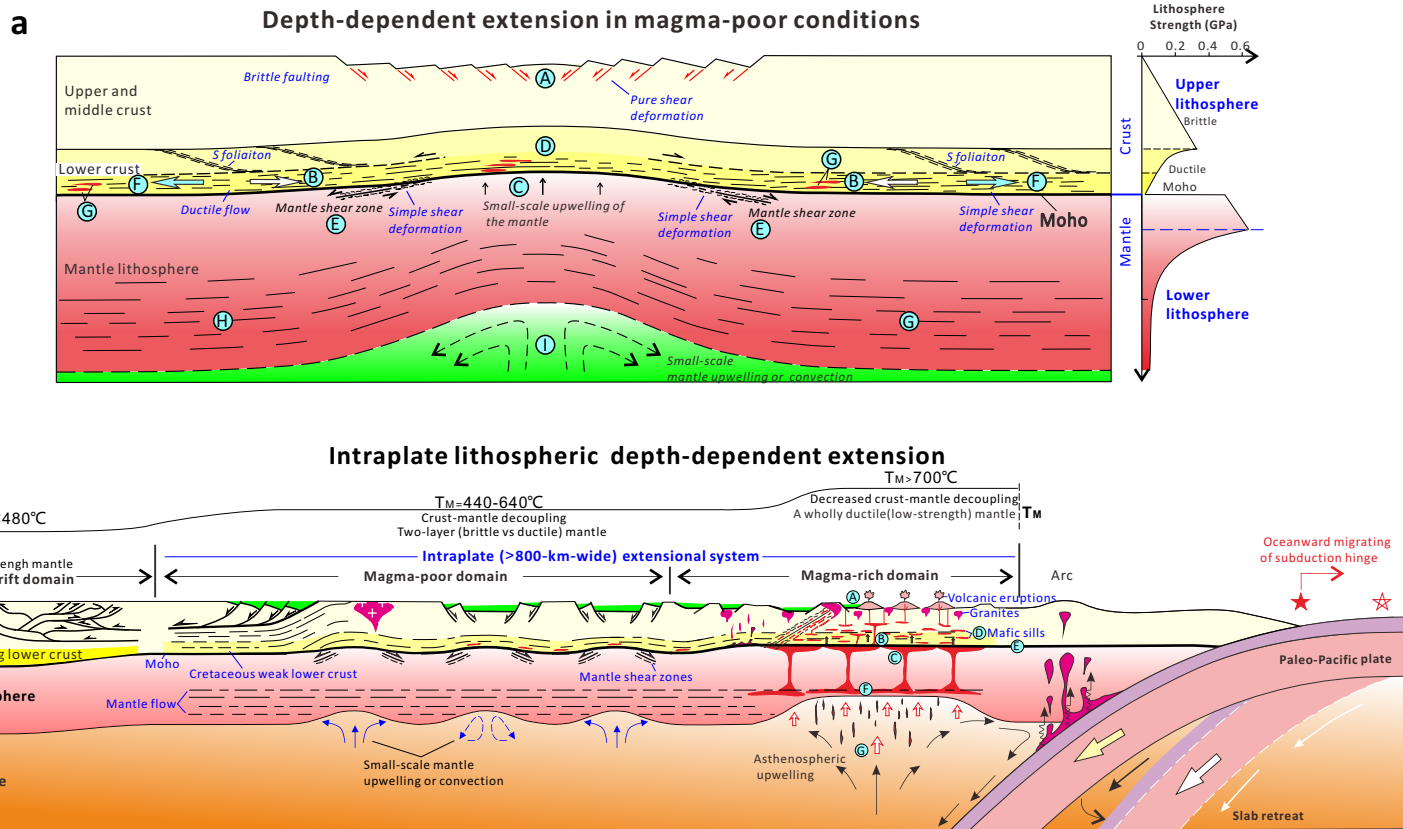


Fig. 5 Model of depth-dependent lithospheric extension for the intraplate extensional system. a, Four-layered, depth-dependent extension of the lithosphere in magma-poor conditions. The right side shows the schematic illustration of maximum rock strength as a function of depth for the continental lithosphere, from ref. 50. The depth-dependent extension appears to evolve in a combined manner of pure- and simple- shear; the upper crust underwent stretching via pure shear, whereas simple shear dominated lateral flow in the lower crust and localized extension in the uppermost mantle. A-F illustrate two stages of the depth-dependent extension (see text for their typical characteristics). **b**, Configuration of lateral variation in modes of depth-dependent extension across the intraplate extensional system. Seismic data supporting this configuration: pre-rift domain, ref. 46; magma-poor domain, this study; magma-rich domain, ref. 43.

Supplementary Files

This is a list of supplementary files associated with this preprint. Click to download.

- [SUPPLEMENTARYINFORMATIONfinal.pdf](#)